
OBPOSE: Leveraging Canonical Pose for Object-Centric Scene Inference in 3D

Yizhe Wu
Applied AI Lab
University of Oxford
Oxford, UK
ywu@robots.ox.ac.uk

Oiwi Parker Jones
Applied AI Lab
University of Oxford
Oxford, UK
oiwi@robots.ox.ac.uk

Ingmar Posner
Applied AI Lab
University of Oxford
Oxford, UK
ingmar@robots.ox.ac.uk

Abstract

We present OBPOSE, an unsupervised object-centric generative model that learns to segment 3D objects from RGB-D video in an unsupervised manner. Inspired by prior art in 2D representation learning, OBPOSE considers a factorised latent space, separately encoding object-wise location (*where*) and appearance (*what*) information. In particular, OBPOSE leverages an object’s *canonical pose*, defined via a minimum volume principle, as a novel inductive bias for learning the *where* component. To achieve this, we propose an efficient, voxelised approximation approach to recover the object shape directly from a neural radiance field (NeRF). As a consequence, OBPOSE models scenes as compositions of NeRFs representing individual objects. When evaluated on the YCB dataset for unsupervised scene segmentation, OBPOSE outperforms the current state-of-the-art in 3D scene inference (ObSuRF) by a significant margin in terms of segmentation quality for both video inputs as well as for multi-view static scenes. In addition, the design choices made in the OBPOSE encoder are validated with relevant ablations.

1 Introduction

In recent years, object-centric representations have emerged as a paradigm shift in machine perception. Intuitively, inference or prediction tasks in down-stream applications are significantly simplified by reducing the dimensionality of the hypothesis space from raw perceptual inputs, such as pixels or point-clouds, to something more akin to a traditional state-space representation. While reasoning over objects rather than pixels has long been the aspiration of machine vision research, it is the ability to learn such a representation in an unsupervised, generative way that unlocks the use of large-scale, unlabelled data for this purpose. As a consequence, research into object-centric generative models (OCGMs) is rapidly gathering pace.

Central to the success of an OCGM are the inductive biases used to encourage the decomposition of a scene into its constituent components. With the field still largely in its infancy, much of the work to date has confined itself to 2D scene observations to achieve both scene inference [e.g. 1, 2, 3, 4, 5, 6, 7] and, in some cases, generation [e.g. 6, 7]. In contrast, unsupervised methods for object-centric scene decomposition operating directly on 3D inputs remain comparatively unexplored [8, 9] – despite the benefits due to the added information contained in the input. As a case in point, Stelzner et al. [9] recently established that access to 3D information significantly speeds up learning. Another benefit is that, for the parts of an object visible to a 3D sensor, object *shape* is readily accessible and does not have to be inferred either from a single view [e.g. 10, 11] or from multiple views [e.g. 12, 13]. Here we conjecture that object shape can serve as a highly informative inductive bias for object-centric learning. Irregular shape can be used to discover an object’s pose and pose can help to identify and locate objects in space.

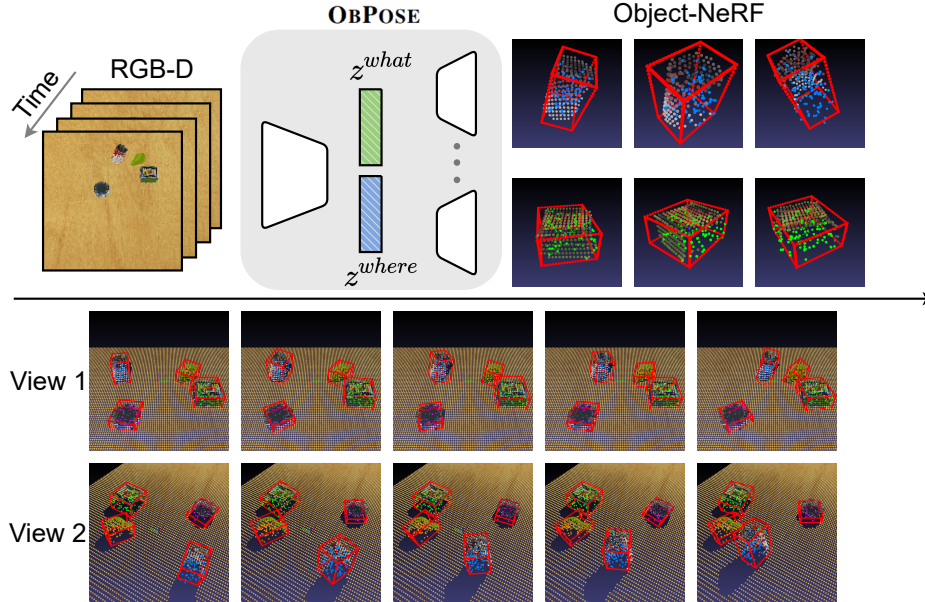


Figure 1: Overview. OBPOSE takes input of a front-view video; it reconstructs the sparse voxelised point cloud and the recovered *canonical pose* of each object. Each point within a distinct slot is coloured to represent a distinct object.

We present OBPOSE, an unsupervised OCGM that takes RGB-D video as input and learns to segment the underlying scene into its constituent 3D objects and a background. Inspired by prior art in 2D settings [1, 14, 15, 16, 17, 18], OBPOSE factorises its latent embedding into a component capturing an object’s location and appearance (*where* and *what* components, respectively). This factorisation provides a strong inductive bias, helping the model to disentangle its input into meaningful concepts for later use.

A key contribution of OBPOSE is the introduction of a novel inductive bias, *canonical pose*, which leverages observed and imagined (in occlusions) object shape to inform the learning of the *where* component in 3D. Taking inspiration from the use of canonical pose in the pose estimation literature [e.g. 19], the intuition for OCGMs is that observed differences in object pose should be invariant in the latent space. We propose to infer canonical pose without supervision, using a minimum volume principle defined using the tightest bounding box that constrains an object. In addition, we propose a voxelised approximation approach that recovers an object’s shape, in a computationally tractable way from a neural radiance field (NeRF) [20]. Although the recovery of an object’s shape from a NeRF can be prohibitively expensive, our approach allows this to be integrated efficiently into the OBPOSE training loop.

In a series of experiments, OBPOSE outperforms ObSuRF [9], the current state-of-the-art in 3D scene inference, by significant margins. Evaluations are performed on the YCB dataset for unsupervised scene segmentation [21], using both RGB-D video and multi-view static scenes. Ablations on the OBPOSE encoder validate the design decisions that distinguish its use of attention mechanisms from two alternatives, represented by Slot Attention [5] and GENESIS-v2 [7]. The key contributions of this paper are: (1) a new state-of-the-art unsupervised scene segmentation model for 3D, OBPOSE, together with insights into its design decisions; (2) a novel inductive bias for 3D OCGMs, *canonical pose*; and (3) a general method for fast shape evaluation that enables efficient training.

2 Methods

OBPOSE takes RGB-D videos as input and learns to segment scenes into a set of foreground objects, with a single background component. The location and orientation of objects (i.e. pose) can be estimated based on the objects’ respective shapes, using NeRFs [20]. Each NeRF models an implicit function representation of the 3D geometry and the textures of a scene component. OBPOSE performs

three steps for each video frame observed: First, an instance colouring stick-breaking process (IC-SBP) step is performed which clusters pointwise embeddings, encoded from a KPConv [22] backbone, into soft attention masks of objects. Second, a *where*-inference step is taken that predicts the object locations and orientations according to the object-wise attention masks from the IC-SBP. Finally, a *what*-inference step encodes the appearance and shape information conditioned on the object poses and then decodes these into NeRFs. These are then composed together with the background component to reconstruct the original scene. A schematic overview of the OBPOSE architecture is provided in Figure 2.

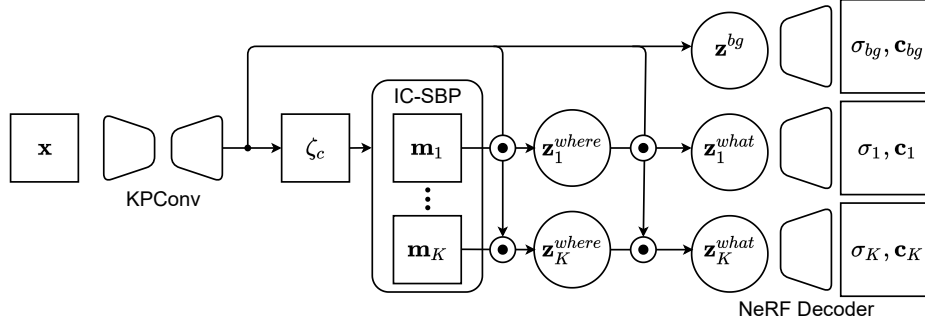


Figure 2: Model architecture. Given an input RGB-D image \mathbf{x} , the KPConv backbone extracts point embeddings ζ_c and a background component \mathbf{z}^{bg} . The point embeddings are clustered by the IC-SBP into soft attention masks, $\mathbf{m}_1 \dots \mathbf{m}_K$, for each object slot. Given these object masks, a *where* module infers the location of each object encoded by \mathbf{z}^{where} . Conditioned on object poses, which are recovered via the minimum volume principle, the *what* latents, \mathbf{z}^{what} , are encoded and then decoded into object NeRFs. Object NeRFs are finally composed with the background component to reconstruct the observed scene.

2.1 Encoder

The input observation x_t is a RGB-D image of height H and width W for each time-step $t \in \{1 \dots T\}$. RGB-D depth images are converted into the point clouds p_t using the known camera parameters (extrinsic and intrinsic). The point clouds p_t and the RGB channels of x_t are then concatenated and encoded into a point embedding $\zeta^{H_1 \times W_1 \times D}$. This is achieved using a U-Net-like backbone module [23] consisting of several KPConv layers [22]. A KPConv layer is an extension of a 2D convolutional neural network (CNN) layer for point clouds, which preserves the translation invariance properties of CNNs. For computational efficiency, output embeddings are upsampled to the resolution of the first downsampled embedding using trilinear interpolation. An aggregation layer is required to summarise the global information for encoding the background information into the latent representation \mathbf{z}^{bg} . For classification tasks, average pooling was adopted for aggregation [22]. However, the pooling is not suitable for capturing the location information of the input features. Instead, we use a KPConv-aggregate layer to aggregate the output features, initialising a convolutional kernel at the coordinate centre. In this way, global spatial information is preserved and encoded in the relative distances between the output features and the kernel points. Following prior work [7], we additionally build two heads upon the output embedding ζ , with one predicting the colour embedding $\zeta_c^{H_1 \times W_1 \times D_c}$ for the IC-SBP, and the other predicting the feature embedding $\zeta_f^{H_1 \times W_1 \times D_f}$ for other encoding tasks.

2.1.1 Instance Colouring Stick-Breaking Process for Video

An instance colouring stick-breaking process (IC-SBP) takes point embeddings $\zeta_c^{H_1 \times W_1 \times D_c}$ as inputs and outputs K predicted soft attention masks $\mathbf{m}_k \in [0, 1]^{H_1 \times W_1}$. The stick-breaking process [2] guarantees that the masks are normalised:

$$\mathbf{m}_1 = \alpha_1, \quad \mathbf{m}_k = \mathbf{s}_{k-1} \odot \alpha_k, \quad \mathbf{m}_K = \mathbf{s}_K, \quad (1)$$

where the *scope* $\mathbf{s}_k \in [0, 1]^{H_1 \times W_1}$ tracks which pixels have not yet been explained. \mathbf{s}_k is initialised and updated as follows:

$$\mathbf{s}_0 = \mathbb{1}^{H_1 \times W_1}, \quad \mathbf{s}_k = \mathbf{s}_{k-1} \odot (1 - \alpha_k) \quad (2)$$

The alpha mask α_k is computed as the distance between a cluster seed $\zeta_{i,j}$ and all individual point embeddings according to a kernel ψ . Readers are referred to the relevant literature [7] for details on kernel selection; our implementation uses Gaussian kernels. The IC-SBP prevents the model from learning a fixed order of decomposition. It achieves this by selecting the cluster seed at the spatial location (i, j) according to the argmax of a score mask $\mathbf{s}_k^c = \mathbf{s}_k \odot \mathbf{u}$ with \mathbf{u} being a score map sampled from a uniform distribution $U(0, 1)^{H_1 \times W_1}$. The score map \mathbf{u} ensures the stochastic ordering of the mask \mathbf{m}_k .

Although the IC-SBP is by default agnostic with respect to the slots, there are nonetheless special components in scene segmentation such as the background. We model slots like these that contain special components by passing the pixel embeddings $\zeta_c^{H_1 \times W_1 \times D_c}$ through a multilayer perceptron (MLP) ρ to compute a pre-scope \mathbf{s}^p :

$$\mathbf{s}^p = \underset{K'}{\text{softmax}}(\rho(\zeta) \in \mathbb{R}^{H_1 \times W_1 \times K'}) \quad (3)$$

Here $K' - 1$ is the number of special slots. By convention we take the last channel of \mathbf{s}^p to be the *scope* \mathbf{s}_0 in the IC-SBP. In the present study, we set $K' = 2$ for only modelling the background. A termination mechanism is implemented by sampling from the remaining scope \mathbf{s}_k before computing the alpha mask α_k at each step k . Each point in the scope \mathbf{s}_k is treated as an independent Bernoulli distribution with the probabilities being the scope value and perform point-wise sampling. The current slot is set to the idle state when all sampled values are zero, which indicates that the whole observation has been explained by previous slots. This contrasts with prior work where a termination condition is proposed to indicate when the IC-SBP should stop [7].

For the video input, we extend the original IC-SBP to include an additional propagation step. The cluster seed $\zeta_{i,j}$ can be used as an ID for each slot throughout the video. The cluster seed sampled at $t = 1$ is stored and used to compute the alpha masks for frames of $t \geq 2$. The idle slots detected at $t = 1$ will remain in idle states during propagation. To ensure the normalisation of the masks \mathbf{m}_k , the SBP operation of IC-SBP takes the remaining scope \mathbf{s}_K as the last component mask \mathbf{m}_K . This does not have an associated seed for propagation. We run one more step of the SBP for the last component and flag the remaining scope \mathbf{s}_K as unused. Concretely, we add an additional penalty loss to encourage the final remaining scope \mathbf{s}_K to be zero everywhere, thereby motivating the model to explain the whole observation using only the previous slots.

2.1.2 Canonical Pose Conditioned Encoding

Pose-invariance is a valuable property in a latent space focused on objects. To evaluate the pose, we note that the point cloud can be viewed as a discrete sampling from the object surface and thus preserves the shape information of the objects. A *canonical pose* can be defined given that $\mathbf{P}_{t,k} = \{\mathbf{p}_j | j \in \{1, \dots, N_k\}\}$ is a set of points that approximates the 3D shape of object k at time step t . Intuitively, the location of the object $\mathbf{T}_{t,k}$ can be initialised at the centre of mass of $\mathbf{P}_{t,k}$:

$$\mathbf{T}_{t,k} = \frac{1}{N_k} \sum_{j \in \{1, \dots, N_k\}} \mathbf{p}_j \quad (4)$$

with N_k being the number of points of object k . For the orientation of the object, which can be represented by a rotation matrix $\mathbf{R}_{t,k} \in \text{SO}(3)$, we propose the following *minimum volume principle* to define a unique shape-based object orientation: given a set of points, we set the canonical orientation of the object represented by those points to the orientation of the tightest bounding box that contains those points. Concretely, we find this bounding box by first transforming the points under several selection rotation matrices $\mathbf{R}^s \in \text{SO}(3)$ and then computing the volume of the axis-aligned bounding boxes (AABBs) that contain these points. Selection rotation matrices are generated as equivolumetric grids in the $\text{SO}(3)$ manifold [24, 25]. This method is based on the HEALPix method of generating equal area grids on the 2-sphere [26]. Due to the symmetry property of the bounding boxes, the smallest bounding box can have multiple solutions, e.g. swapping the x-axis and the y-axis of the coordinates of the bounding box will result in another bounding box that has the same volume. Therefore, we select all the bounding boxes whose volumes are in the range $[V_{\min}, (1 + \beta)V_{\min}]$ to account for this issue, where V_{\min} is the minimum volume of all the AABBs and β is a small tolerance factor. We pick the AABB whose orientation is closest to the world coordinates and whose orientation is represented by the identity matrix $\mathbf{I} \in \mathbb{R}^{3 \times 3}$. The distance $d_{\text{SO}(3)}$ is measured by the

geodesic distance on the $SO(3)$ manifold:

$$d_{SO(3)} = \arccos\left(\frac{\text{tr}(\mathbf{R}_{t,k}) - 1}{2}\right) \quad (5)$$

The points \mathbf{p}_j are then transformed to their canonical coordinates given a pair of pose parameters $\{\mathbf{T}, \mathbf{R}\}$ as follows:

$$k(\mathbf{p}_j, \mathbf{R}, \mathbf{T}) = \frac{2}{s}(\mathbf{R})^{-1}(\mathbf{p}_j - \mathbf{T}) \quad (6)$$

The bounding box size $s \in \mathbb{R}$ is initialised to a sufficiently large number for all objects. All points that are out of the bounding box are discarded so that the spatial coordinate of each point is in the range of $[-1, 1]$.

For each object slot at time step t , we find its associated point cloud $\mathbf{P}_{t,k}$ by computing the argmax over the attention masks $\mathbf{m}_{t,k}$ predicted from the IC-SBP. The point features $\zeta_{f,t}$ at time step t are also masked by the attention masks, i.e. $\zeta_{t,k} = \zeta_{f,t} \odot \text{detach}(\mathbf{m}_{t,k})$. The object location $\mathbf{T}_{t,k}$ estimated from the observed points $\mathbf{P}_{t,k}$ is, however, biased toward object surface as the object is only partially observed. We thus use a *where* module that takes $\mathbf{P}_{t,k}$ and $\zeta_{t,k}$ as input and predicts a $\Delta\mathbf{T}_{t,k}$ to correct the bias. To learn a relative translation we first transform $\mathbf{P}_{t,k}$ using the pose parameters $\{\mathbf{T}_{t,k}, \mathbf{I}\}$ as in eq. (6). Concretely, the *where* module is an encoder that consists of several KPConv layers and a KPConv-aggregate layer as the final output layer. The encoded embedding is then fed to a recurrent neural network (RNN) with its hidden states later being decoded into the mean and standard deviation of the posterior distribution $q(\mathbf{z}_{t,k}^{\text{where}} | x_{\leq t})$ parameterised as a Gaussian. The $\mathbf{z}_{t,k}^{\text{where}}$ is decoded to the $\Delta\mathbf{T}_{t,k}$ through an MLP f^{where} such that:

$$\Delta\mathbf{T}_{t,k} = T_{\max} \tanh(f^{\text{where}}(\mathbf{z}_{t,k}^{\text{where}})) \quad (7)$$

with $T_{\max} \in \mathbb{R}$ being the maximum delta translation. Given the updated object location $\hat{\mathbf{T}}_{t,k} = \mathbf{T}_{t,k} + \Delta\mathbf{T}_{t,k}$, we encode the shape and the appearance of the object from the observations transformed in the canonical pose $\{\hat{\mathbf{T}}_{t,k}, \mathbf{R}_{t,k}\}$. Similar to the *where* module, the posterior distribution $q(\mathbf{z}_{t,k}^{\text{what}} | \mathbf{z}_{\leq t,k}, x_{\leq t})$ is also parameterised by a KPConv encoder appended by an RNN. If the point number N_k is small, we instead initialise the canonical pose $\mathbf{T}_{t,k}, \mathbf{R}_{t,k}$ with the object location from the last time step, i.e. $\{\hat{\mathbf{T}}_{t-1,k}, \mathbf{I}\}$ during the propagation.

We use two RNN networks to model the prior distributions $p(\mathbf{z}_{t,k}^{\text{where}} | \mathbf{z}_{<t,k}^{\text{where}})$ and $p(\mathbf{z}_{t,k}^{\text{what}} | \mathbf{z}_{<t,k}^{\text{what}})$, whose hidden states are decoded by an MLP to the mean and standard deviation. The prior distribution at $t = 0$ are Gaussian distributions of zero mean for both the $\mathbf{z}^{\text{where}}$ and the \mathbf{z}^{what} .

2.2 Decoder

To explicitly model the 3D geometry of scenes, we represent each object and the background as a Neural Radiance Field (NeRF) [20]. Each NeRF is a function parameterised by an MLP that maps the world coordinates \mathbf{p} and the viewing direction \mathbf{d} to a color value \mathbf{c} and a density value σ . One limitation is that a given NeRF can only represent a single scene and cannot condition on the latent encoding. The approach has therefore been extended [27, 28] to learn the mapping $f: (\mathbf{p}, \mathbf{d}, \mathbf{z}) \rightarrow (\mathbf{c}, \sigma)$. This introduces a mapping from the latent encoding \mathbf{z} to modifications to the hidden layer outputs of the NeRF MLP. To compose the individual NeRFs into a single scene function, previous approaches [9, 28] combine the density values by a summation operation, i.e. $\sigma = \sum_{k=1}^K \sigma_k$. This way of composing NeRFs is equal to a superposition of independent Poisson point processes [9]. The scene colour can then be computed as a weighted mean $\mathbf{c} = \frac{1}{\sigma} \sum_{k=1}^K \sigma_k \mathbf{c}_k$. We know that a voxel should not be occupied by multiple objects. To account for this property, [9] proposes an auxiliary loss to penalize the difference between the sum of the density values and the maximum density values of all components, as simply composing NeRFs with a summation does not suffice. This auxiliary loss, however, requires a warm-up training strategy and introduces additional hyper-parameters for different datasets. We thus propose to model the scene function as:

$$\sigma = \sigma_{\max} \tanh\left(\sum_1^k \text{softplus}(\sigma_k)\right), \hat{\sigma}_k = \sigma \text{softmax}_K(\sigma_k) \quad (8)$$

In our case, σ_k can be interpreted as the logits of the probability, indicating whether this voxel is occupied or not, and $\hat{\sigma}_k$ is the normalised density with a range of $[0, \sigma_{\max}]$. For the colours, we can

compute the weighted mean: $\mathbf{c} = \frac{1}{\sigma_{\max}} \sum_1^K \hat{\sigma}_k \mathbf{c}_k$. We upper bound the density by $\sigma_{\max} \in \mathbb{R}$ and model the probability of whether the voxel has been occupied through a tanh. The softplus function ensures that no component can contribute negative occupancy. We use the softmax function to account for the fact that the objects should not overlap, without needing to introduce extra hyper-parameters. To estimate the shape of the objects reconstructed from the NeRFs, we would like a fast approximation approach, as the full evaluation of the volumetric rendering is computationally expensive. Inspired by prior work [29], we divide each object bounding box into \mathbf{S} sparse voxels along each dimension. The occupancy at these voxel centres \mathbf{p}_v can then be evaluated by $\sigma_v = \tanh(\text{softplus}(f(\mathbf{p}_v, \mathbf{z}_k)))$. We denote the voxels as occupied if $\sigma_v > \sigma_T$, with the σ_T being a threshold. Given the set of the occupied voxels and their centre positions \mathbf{p}_v , we can recover the canonical object centre $\mathbf{T}_{t,k}^{\text{shape}}$ and the object orientation $\mathbf{R}_{t,k}^{\text{shape}}$ as discussed in 2.1.2.

3 Training

Training a NeRF with known depth requires relatively few evaluations. Stelzner et al. [9], for example, propose to use only two evaluations of the NeRF for each training iteration, i.e. one evaluation at the surface and one evaluation at points between the camera and the surface. To avoid learning an extremely thin surface, the points sampled at the surface are sampled between the depth range $[\mathbf{d}_{\text{surface}}, \mathbf{d}_{\text{surface}} + \delta]$, with the δ denoting the surface thickness. The observation loss can be divided into two terms, i.e. a texture loss term:

$$\mathcal{L}_{\text{colour}} = -\log\left(\sum_{k=1}^K \mathcal{N}(\mathbf{c}_k, \sigma_{\text{std}}) \odot \hat{\sigma}_k^{\text{surface}} / \sigma_{\max}\right) \quad (9)$$

with σ_{std} denoting a fixed standard deviation, and a depth loss term [9]:

$$\mathcal{L}_{\text{depth}} = -\log(\sigma(\mathbf{p}^{\text{surface}})) + \sigma(\mathbf{p}^{\text{air}}) / \rho^{\text{air}} \quad (10)$$

where ρ^{air} is a probability density of the point \mathbf{p}^{air} being sampled. The latent embedding is regularized using the KL term:

$$\mathcal{L}_{\text{KL}} = \mathbb{KL}(q_{\phi}(\mathbf{z}_t | \mathbf{z}_{\leq t}, \mathbf{x}_{\leq t}) || p_{\theta}(\mathbf{z}_t | \mathbf{z}_{< t})) \quad (11)$$

An L_2 loss is used to supervise the *where* module:

$$\mathcal{L}_{\text{where}} = \sum_k (\hat{\mathbf{T}}_{t,k} - \mathbf{T}_{t,k}^{\text{shape}})^2 \quad (12)$$

For the attention mask of the IC-SBP, the learning of the attention masks is supervised via:

$$\mathcal{L}_{\text{att}} = -(\log(\sum_{k=1}^K \mathbf{m}_k \odot (\mathcal{N}(\mathbf{c}_k, \sigma_{\text{std}}) \odot \hat{\sigma}_k^{\text{surface}} / \sigma_{\max}))) + \log(\sum_{k=1}^K \mathbf{m}_k \odot \hat{\sigma}_k^{\text{surface}} / \sigma_{\max}) \quad (13)$$

In the end, we penalise the remaining scope \mathbf{s}_K by introducing the remaining scope loss:

$$\mathcal{L}_{\text{scope}} = \sum_{i=1}^{H_1} \sum_{j=1}^{W_1} s_{K,i,j} \quad (14)$$

Taken together, these losses lead to the overall loss:

$$\mathcal{L} = \mathcal{L}_{\text{colour}} + \mathcal{L}_{\text{depth}} + \mathcal{L}_{\text{KL}} + \mathcal{L}_{\text{where}} + \mathcal{L}_{\text{att}} + \mathcal{L}_{\text{scope}} \quad (15)$$

For the training, we use the Adam optimizer with a fixed learning rate of $4e^{-4}$ and without any learning rate warm-up or decay strategy.

4 Experiments

To evaluate OBPOSE’s performance on unsupervised segmentation tasks of 3D scenes and to demonstrate its ability to estimate 6D poses of objects, we conduct experiments on two YCB object datasets [21]. One is a video dataset of RGB-D images captured from a fixed front view and another is a dataset of static images captured from three different points of view. The three views are obtained by

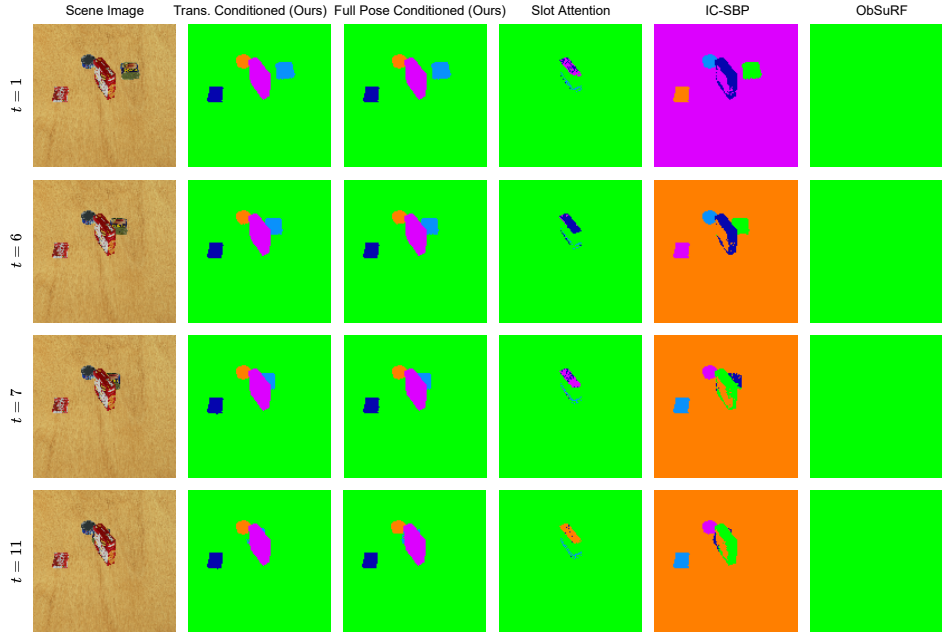


Figure 3: Visualisation of the segmentation results using the YCB video dataset. Our model (OBPOSE) learns better segmentations in the demonstrated video. Each slot is associated with a fixed colour throughout the video. The colours are chosen to be visually distinct from one another.

rotating the camera by $120^\circ/240^\circ$ around the z-axis of the world frame. All images are shuffled so that ground-truth pairing information is not used for training. In each dataset, two to four randomly selected objects are spawned on the table. The metrics used for evaluation are described below. Performance is compared against the recent baseline of ObSuRF [9], which, to the best of our knowledge, is the only unsupervised scene segmentation model that operates on RGB-D images of 3D scenes. To validate our model design decisions, we also compare performance using different attention mechanisms on the encoder side, i.e. slot attention [5] and IC-SBP [7] with an object encoder that does not model object pose. In addition, we also compare two ablations of the OBPOSE encoder, i.e. one conditioned only on the locations of the objects and one conditioned on the full 6D poses.

4.1 Metrics

Segmentation quality is quantified using the Adjusted Rand Index (ARI) [30, 31] and Mean Segmentation Covering (MSC) as metrics. In contrast to mean Intersection over Union (mIoU), ARI measures the clustering similarity between the predicted segmentation masks and the ground-truth segmentation masks in a permutation-invariant fashion. This is suitable for unsupervised segmentation approaches as there are no fixed associations between slots and objects. We evaluate segmentation accuracy on foreground objects using the foreground-only ARI and MSC (denoted ARI-FG and MSC-FG, respectively), and on the background using mIoU. All metrics are normalised with possible values ranging between 0 and 1, where a score of 1 indicates perfect segmentation.

4.2 Unsupervised 3D Object Segmentation

Qualitative results on the YCB video dataset are depicted in Figure 3. Quantitative segmentation results are additionally summarised in Table 1. Taking these in turn, we first observe that the ObSuRF baseline fails to segment the scenes properly using the default setting for 3D data from the open-sourced code. This might be attributed to the weight of a overlap loss used in ObSuRF, to discourage the objects from overlapping. In Stelzner et al. [9] the same failure mode is reported and thus a warm-up of the weight is carefully chosen for training. In OBPOSE, we instead use the *softmax* function in Equation (8). This provides an inductive bias without hyper-parameters, alleviating the computationally expensive hyper-parameter searching process. Interestingly, using the full 6D pose including the orientation and the location of the objects does not strongly affect the

Table 1: Mean and standard deviation of the segmentation metrics on the YCB video dataset and the YCB static dataset from three random seeds. The results are rounded to two decimal places. OBPOSE outperforms the baseline and the ablations as it explicitly estimates the *canonical poses* of the objects, disentangling object location and appearance.

	YCB Video			YCB Static		
	mIoU-BG \uparrow	ARI-FG \uparrow	MSC-FG \uparrow	mIoU-BG \uparrow	ARI-FG \uparrow	MSC-FG \uparrow
OBSURF	0.96 \pm 0.00	0.00 \pm 0.00	0.00 \pm 0.00	0.92 \pm 0.00	0.00 \pm 0.00	0.00 \pm 0.00
SLOT ATT. *	0.98 \pm 0.02	0.13 \pm 0.05	0.19 \pm 0.02	1.00 \pm 0.00	0.80 \pm 0.01	0.84 \pm 0.00
IC-SBP	0.96 \pm 0.05	0.87 \pm 0.02	0.90 \pm 0.02	0.97 \pm 0.03	0.83 \pm 0.09	0.80 \pm 0.15
OBPOSE (ours)	1.00 \pm 0.00	0.96 \pm 0.00	0.97 \pm 0.00	0.99 \pm 0.00	0.89 \pm 0.01	0.87 \pm 0.03
OBPOSE + ROT. (ours)	1.00 \pm 0.00	0.96 \pm 0.00	0.97 \pm 0.00	0.98 \pm 0.00	0.88 \pm 0.01	0.84 \pm 0.03

* The SLOT ATT results are computed with one failed random seed being excluded for the YCB static dataset.

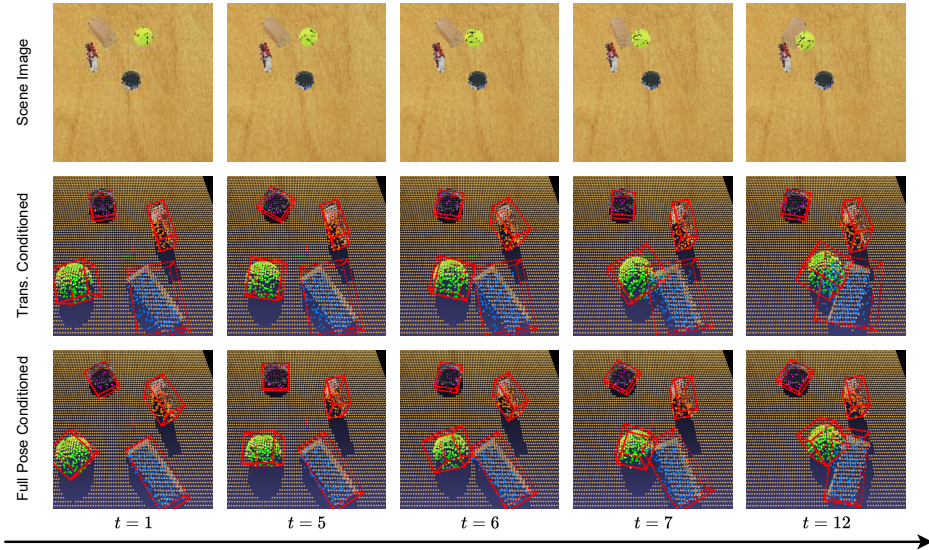


Figure 4: Visualisation of the voxelised shape reconstruction for each object, and for the recovered bounding boxes estimated from the reconstructed object shape, as viewed from the back side of the scene. The centres of the occupied voxels of each object are shown in distinct colours. The object-centric NeRFs learn to interpolate the inner body of the objects with high density predictions.

segmentation performance compared to using only the object positions as a way to condition the encoding. This suggests that for object segmentation tasks, the object location itself already provides a strong inductive bias for successful decomposition. Similar results are observed elsewhere in the literature [32], where simple ground-truth position information for objects is used in the first video frame, allowing the model to perform scene segmentation of 2D video data in a weakly supervised fashion. In our approach, we explicitly leverage the 3D reconstruction of the objects whose shape is estimated by the proposed voxelised shape approximation approach. This allows the model to infer the canonical poses of objects in a computationally efficient way without using any ground-truth labels. OBPOSE also achieves lower variation on metrics for both datasets, suggesting more stable training compared to the original IC-SBP.

4.3 Unsupervised 6D Pose Estimation and Shape Completion with Object-centric NeRFs

The unsupervised 6D pose estimation results are illustrated in Figure 4. In our model, the locations of objects are predicted directly as the outputs of the *where* module, whereas the orientations are estimated by the proposed minimum volume principle (Section 2.1.2). Evaluating the locations and orientations of objects requires a set of sparse points in 3D that approximate the objects’ shapes. To achieve this, we could either mask out the observed point cloud with the attention masks predicted from the IC-SBP, or we could use the voxelised shape approximation computed in the decoder step as the shape approximation. The former method provides the model with a stable shape signal, as it

relates directly to the ground-truth observations; this method is used in the full 6D pose conditioned encoding ablation for robust training. On the other hand, the latter method reconstructs the full 3D shape of the objects including the unobserved parts, and is thus a more accurate approximation of the object shapes. We therefore use the voxelised shape approximation in the evaluation phase as visualised in Figure 4. We find that the object NeRFs learn to interpolate the inner body of the objects with high occupancy predictions, even though the training signals are preempted near the object surface due to the volume rendering. This property of NeRFs allows us to estimate accurate centres of mass and object orientations. We further observe that on the YCB video data, where all observations are captured from a single front view, the object NeRFs can still reconstruct the unobserved back side of the objects. In most NeRF applications, a multiple-view setting with known camera parameters is usually assumed. However, our work indicates the possibility of applying NeRFs in scenes observed from a single view, where objects are moving but the camera is fixed. Such a setting has potential for applications such as robot grasping tasks, where a camera is commonly positioned in front of a table.

5 Related Work

OBPOSE builds upon prior OCGM work on unsupervised segmentation in both 2D and 3D. It is also related conceptually to previous work on canonical pose, in supervised and unsupervised settings.

Most OCGMs for 2D scene segmentation are formulated as variational autoencoders (VAEs) [33, 34], where different likelihood models serve to explain observations. One set of VAE-OCGMs use bounding boxes, derived from spatial transformer networks (STNs) to represent (*glimpse*) individual objects [1, 35, 14, 15, 16, 17]. Another set represents objects via unsupervised instance segmentation, using pixel-wise mixture models [2, 6, 36, 3, 4, 37, 38, 39, 5]. This latter set relaxes the spatial-consistency requirements imposed by bounding boxes [40], permitting more flexible modelling of objects with complex shapes and textures. However, relaxing spatial consistency has the side-effect that performance can sometimes be biased by features such as the colour of the object [41], which has motivated the search for additional inductive biases. A promising candidate is temporal information. To this end, some works [39, 42, 32] operate on video data and model the correlations between objects explicitly using graph neural networks (GNNs) [43, 44] or Transformers [45].

With the advent of differentiable rendering techniques [10, 20], recent works have begun to model the observed scene directly in 3D [46, 28, 9, 12]. This leads to improved data-efficiency as the rendering process accounts for spatial relationships such as occlusions without the requirement of learning these effects from data. Work on unsupervised 3D scene segmentation has learned from multiple static images or RGB-D images of scenes, not previously from video.

The idea of a canonical pose, or reference pose for an object, has precedent in the context of 6D pose estimation, which aims to find the translation and rotation of an object with respect to some frame of reference. In the supervised setting, labels are defined with respect to a given canonical frame [19, 47, 48, 49, 50, 51]. Recently, it has been shown that pose between views of an object, or objects from a common category, can be inferred without labels. Such relative poses have been found for point clouds [52] and RGB-D images [53]. To the best of our knowledge, we are the first to propose a minimum volume approach for discovering canonical pose without supervision and to use canonical pose as an inductive bias.

6 Conclusion

We present OBPOSE, an object-centric generative model that is able to decompose 3D scenes into objects and background, with each object being represented as a NeRF. OBPOSE extends IC-SBP for video data and introduces *canonical poses* of objects as a powerful inductive bias for unsupervised segmentation. Learning object locations is facilitated by a number of recent developments: the implicit function representations of the 3D shapes and the fast voxelised shape approximation proposed in this paper. Our experimental results are validated on two established synthetic YCB objects datasets (static 3D and video). Given its empirical success, outperforming the prior state-of-the-art for static 3D scenes [9] and establishing a baseline for video, we plan to apply OBPOSE as a vision backbone for robot applications.

Acknowledgments and Disclosure of Funding

This work was supported by EPSRC Programme Grant(EP/V000748/1), an Amazon Research Award and the China Scholarship Council. The authors would like to acknowledge the use of the University of Oxford Advanced Research Computing (ARC) facility in carrying out this work. <http://dx.doi.org/10.5281/zenodo.22558>. They also thank Walter Goodwin, Alexander Mitchell, Frederik Nolte, and Jack Collins for proofreading their work.

References

- [1] SM Eslami, Nicolas Heess, Theophane Weber, Yuval Tassa, David Szepesvari, Geoffrey E Hinton, et al. Attend, infer, repeat: Fast scene understanding with generative models. *Advances in Neural Information Processing Systems (NeurIPS)*, 29, 2016.
- [2] Christopher P Burgess, Loic Matthey, Nicholas Watters, Rishabh Kabra, Irina Higgins, Matt Botvinick, and Alexander Lerchner. MONet: Unsupervised scene decomposition and representation. *arXiv preprint arXiv:1901.11390*, 2019.
- [3] Klaus Greff, Antti Rasmus, Mathias Berglund, Tele Hao, Harri Valpola, and Jürgen Schmidhuber. Tagger: Deep unsupervised perceptual grouping. *Advances in Neural Information Processing Systems (NeurIPS)*, 29, 2016.
- [4] Klaus Greff, Sjoerd Van Steenkiste, and Jürgen Schmidhuber. Neural expectation maximization. *Advances in Neural Information Processing Systems (NeurIPS)*, 30, 2017.
- [5] Francesco Locatello, Dirk Weissenborn, Thomas Unterthiner, Aravindh Mahendran, Georg Heigold, Jakob Uszkoreit, Alexey Dosovitskiy, and Thomas Kipf. Object-centric learning with slot attention. *Advances in Neural Information Processing Systems (NeurIPS)*, 33:11525–11538, 2020.
- [6] Martin Engelcke, Adam R Kosiorek, Oiwi Parker Jones, and Ingmar Posner. GENESIS: Generative scene inference and sampling with object-centric latent representations. *arXiv preprint arXiv:1907.13052*, 2019.
- [7] Martin Engelcke, Oiwi Parker Jones, and Ingmar Posner. GENESIS-v2: Inferring unordered object representations without iterative refinement. *Advances in Neural Information Processing Systems (NeurIPS)*, 34, 2021.
- [8] Cathrin Elich, Martin R. Oswald, Marc Pollefeys, and Joerg Stueckler. Weakly supervised learning of multi-object 3d scene decompositions using deep shape priors. *Computer Vision and Image Understanding*, 220:103440, 2022.
- [9] Karl Stelzner, Kristian Kersting, and Adam R Kosiorek. Decomposing 3d scenes into objects via unsupervised volume segmentation. *arXiv preprint arXiv:2104.01148*, 2021.
- [10] Shichen Liu, Tianye Li, Weikai Chen, and Hao Li. Soft rasterizer: A differentiable renderer for image-based 3d reasoning. In *Proceedings of the IEEE/CVF International Conference on Computer Vision*, pages 7708–7717, 2019.
- [11] Hiroharu Kato, Yoshitaka Ushiku, and Tatsuya Harada. Neural 3d mesh renderer. In *Proceedings of the IEEE conference on computer vision and pattern recognition*, pages 3907–3916, 2018.
- [12] Hong-Xing Yu, Leonidas J Guibas, and Jiajun Wu. Unsupervised discovery of object radiance fields. *arXiv preprint arXiv:2107.07905*, 2021.
- [13] Haozhe Xie, Hongxun Yao, Xiaoshuai Sun, Shangchen Zhou, and Shengping Zhang. Pix2vox: Context-aware 3d reconstruction from single and multi-view images. In *Proceedings of the IEEE/CVF International Conference on Computer Vision*, pages 2690–2698, 2019.
- [14] Eric Crawford and Joelle Pineau. Spatially invariant unsupervised object detection with convolutional neural networks. In *Proceedings of the AAAI Conference on Artificial Intelligence*, volume 33, pages 3412–3420, 2019.

- [15] Zhixuan Lin, Yi-Fu Wu, Skand Vishwanath Peri, Weihao Sun, Gautam Singh, Fei Deng, Jindong Jiang, and Sungjin Ahn. SPACE: Unsupervised object-oriented scene representation via spatial attention and decomposition. *arXiv preprint arXiv:2001.02407*, 2020.
- [16] Adam Kosior, Hyunjik Kim, Yee Whye Teh, and Ingmar Posner. Sequential attend, infer, repeat: Generative modelling of moving objects. *Advances in Neural Information Processing Systems (NeurIPS)*, 31, 2018.
- [17] Jindong Jiang, Sepehr Janghorbani, Gerard De Melo, and Sungjin Ahn. SCALOR: Generative world models with scalable object representations. *arXiv preprint arXiv:1910.02384*, 2019.
- [18] Yizhe Wu, Oiwi Parker Jones, Martin Engelcke, and Ingmar Posner. APEX: unsupervised, object-centric scene segmentation and tracking for robot manipulation. *International Conference on Intelligent Robots and Systems (IROS)*, 2021.
- [19] He Wang, Srinath Sridhar, Jingwei Huang, Julien Valentin, Shuran Song, and Leonidas J. Guibas. Normalized object coordinate space for category-level 6d object pose and size estimation. *arXiv preprint arXiv:1901.02970*, 2019.
- [20] Ben Mildenhall, Pratul P Srinivasan, Matthew Tancik, Jonathan T Barron, Ravi Ramamoorthi, and Ren Ng. Nerf: Representing scenes as neural radiance fields for view synthesis. In *European Conference on Computer Vision*, pages 405–421. Springer, 2020.
- [21] Berk Calli, Arjun Singh, Aaron Walsman, Siddhartha Srinivasa, Pieter Abbeel, and Aaron M Dollar. The YCB object and model set: Towards common benchmarks for manipulation research. In *2015 International Conference on Advanced Robotics (ICAR)*, pages 510–517. IEEE, 2015.
- [22] Hugues Thomas, Charles R Qi, Jean-Emmanuel Deschaud, Beatriz Marcotegui, François Goulette, and Leonidas J Guibas. Kpconv: Flexible and deformable convolution for point clouds. In *Proceedings of the IEEE/CVF international conference on computer vision*, pages 6411–6420, 2019.
- [23] Olaf Ronneberger, Philipp Fischer, and Thomas Brox. U-net: Convolutional networks for biomedical image segmentation. In *International Conference on Medical image computing and computer-assisted intervention*, pages 234–241. Springer, 2015.
- [24] Kieran Murphy, Carlos Esteves, Varun Jampani, Srikumar Ramalingam, and Ameesh Makadia. Implicit-pdf: Non-parametric representation of probability distributions on the rotation manifold. *arXiv preprint arXiv:2106.05965*, 2021.
- [25] Anna Yershova, Swati Jain, Steven M Lavalley, and Julie C Mitchell. Generating uniform incremental grids on SO(3) using the Hopf fibration. *The International Journal of Robotics Research*, 29(7):801–812, 2010.
- [26] Krzysztof M Gorski, Eric Hivon, Anthony J Banday, Benjamin D Wandelt, Frode K Hansen, Mstvos Reinecke, and Matthia Bartelmann. HEALPix: A framework for high-resolution discretization and fast analysis of data distributed on the sphere. *The Astrophysical Journal*, 622(2):759, 2005.
- [27] Katja Schwarz, Yiyi Liao, Michael Niemeyer, and Andreas Geiger. GRAF: Generative radiance fields for 3d-aware image synthesis. *Advances in Neural Information Processing Systems (NeurIPS)*, 33:20154–20166, 2020.
- [28] Michael Niemeyer and Andreas Geiger. Giraffe: Representing scenes as compositional generative neural feature fields. In *Proceedings of the IEEE/CVF Conference on Computer Vision and Pattern Recognition*, pages 11453–11464, 2021.
- [29] Lingjie Liu, Jiatao Gu, Kyaw Zaw Lin, Tat-Seng Chua, and Christian Theobalt. Neural sparse voxel fields. *Advances in Neural Information Processing Systems (NeurIPS)*, 33:15651–15663, 2020.
- [30] William M Rand. Objective criteria for the evaluation of clustering methods. *Journal of the American Statistical Association*, 66(336):846–850, 1971.

- [31] Lawrence Hubert and Phipps Arabie. Comparing partitions. *Journal of Classification*, 2(1): 193–218, 1985.
- [32] Thomas Kipf, Gamaleldin F Elsayed, Aravindh Mahendran, Austin Stone, Sara Sabour, Georg Heigold, Rico Jonschkowski, Alexey Dosovitskiy, and Klaus Greff. Conditional object-centric learning from video. *arXiv preprint arXiv:2111.12594*, 2021.
- [33] Diederik P Kingma and Max Welling. Auto-encoding variational bayes. *arXiv preprint arXiv:1312.6114*, 2013.
- [34] Danilo Jimenez Rezende, Shakir Mohamed, and Daan Wierstra. Stochastic backpropagation and approximate inference in deep generative models. In *International Conference on Machine Learning*, pages 1278–1286. PMLR, 2014.
- [35] Taufik Xu, Chongxuan Li, Jun Zhu, and Bo Zhang. Multi-objects generation with amortized structural regularization. *Advances in Neural Information Processing Systems (NeurIPS)*, 32, 2019.
- [36] Martin Engelcke, Oiwi Parker Jones, and Ingmar Posner. Reconstruction bottlenecks in object-centric generative models. *arXiv preprint arXiv:2007.06245*, 2020.
- [37] Sjoerd Van Steenkiste, Michael Chang, Klaus Greff, and Jürgen Schmidhuber. Relational neural expectation maximization: Unsupervised discovery of objects and their interactions. *arXiv preprint arXiv:1802.10353*, 2018.
- [38] Klaus Greff, Raphaël Lopez Kaufman, Rishabh Kabra, Nick Watters, Christopher Burgess, Daniel Zoran, Loic Matthey, Matthew Botvinick, and Alexander Lerchner. Multi-object representation learning with iterative variational inference. In *International Conference on Machine Learning*, pages 2424–2433. PMLR, 2019.
- [39] Rishi Veerapaneni, John D Co-Reyes, Michael Chang, Michael Janner, Chelsea Finn, Jiajun Wu, Joshua Tenenbaum, and Sergey Levine. Entity abstraction in visual model-based reinforcement learning. In *Conference on Robot Learning*, pages 1439–1456. PMLR, 2020.
- [40] Max Jaderberg, Karen Simonyan, Andrew Zisserman, et al. Spatial transformer networks. *Advances in Neural Information Processing Systems (NeurIPS)*, 28, 2015.
- [41] Marissa A Weis, Kashyap Chitta, Yash Sharma, Wieland Brendel, Matthias Bethge, Andreas Geiger, and Alexander S Ecker. Unmasking the inductive biases of unsupervised object representations for video sequences. *arXiv preprint arXiv:2006.07034*, 2, 2020.
- [42] Sébastien Ehrhardt, Oliver Groth, Aron Monszpart, Martin Engelcke, Ingmar Posner, Niloy Mitra, and Andrea Vedaldi. RELATE: Physically plausible multi-object scene synthesis using structured latent spaces. *Advances in Neural Information Processing Systems (NeurIPS)*, 33: 11202–11213, 2020.
- [43] Franco Scarselli, Marco Gori, Ah Chung Tsoi, Markus Hagenbuchner, and Gabriele Monfardini. The graph neural network model. *IEEE Transactions on Neural Networks*, 20(1):61–80, 2009.
- [44] Benjamin Sanchez-Lengeling, Emily Reif, Adam Pearce, and Alexander B. Wiltschko. A gentle introduction to graph neural networks. *Distill*, 2021. doi: 10.23915/distill.00033. <https://distill.pub/2021/gnn-intro>.
- [45] Ashish Vaswani, Noam Shazeer, Niki Parmar, Jakob Uszkoreit, Llion Jones, Aidan N Gomez, Łukasz Kaiser, and Illia Polosukhin. Attention is all you need. *Advances in Neural Information Processing Systems (NeurIPS)*, 30, 2017.
- [46] Thu H Nguyen-Phuoc, Christian Richardt, Long Mai, Yongliang Yang, and Niloy Mitra. BlockGAN: Learning 3d object-aware scene representations from unlabelled images. *Advances in Neural Information Processing Systems (NeurIPS)*, 33:6767–6778, 2020.
- [47] Dengsheng Chen, Jun Li, Zheng Wang, and Kai Xu. Learning canonical shape space for category-level 6d object pose and size estimation. *Computer Vision and Pattern Recognition (CVPR)*, pages 11973–11982, 2020.

- [48] Xiaolong Li, He Wang, Li Yi, Leonidas J. Guibas, A. Lynn Abbott, and Shuran Song. Category level articulated object pose estimation. *In Proceedings of the IEEE/CVF Conference on Computer Vision and Pattern Recognition*, pages 3706–3715, 2020.
- [49] Chen Wang, Roberto Martín-Martín, Danfei Xu, Jun Lv, Cewu Lu, Li Fei-Fei, Silvio Savarese, and Yuke Zhu. 6-pack: Category-level 6d pose tracker with anchor-based keypoints. *International Conference on Robotics and Automation (ICRA)*, pages 10059–10066, 2020.
- [50] Xu Chen, Zijian Dong, Jie Song, Andreas Geiger, and Otmar Hilliges. Category level object pose estimation via neural analysis-by-synthesis. *European Conference on Computer Vision*, pages 139–156, 2020.
- [51] Meng Tian, Marcelo H. Ang, and Gim Hee Lee. Shape prior deformation for categorical 6d object pose and size estimation. *European Conference on Computer Vision*, pages 530–546, 2020.
- [52] Xiaolong Li, Yijia Weng, Li Yi, Leonidas Guibas, A Lynn Abbott, Shuran Song, and He Wang. Leveraging $SE(3)$ equivariance for self-supervised category-level object pose estimation. *Advances in Neural Information Processing Systems (NeurIPS)*, 2021.
- [53] Walter Goodwin, Sagar Vaze, Ioannis Havoutis, and Ingmar Posner. Zero-shot category-level object pose estimation. *arXiv preprint arXiv:2204.03635*, 2022.
- [54] Yuxin Wu and Kaiming He. Group normalization. *In Proceedings of the European conference on computer vision (ECCV)*, pages 3–19, 2018.

Appendix

6.1 Minimum Volume Principle in Detail

The proposed approach for recovering the *canonical pose* for an object is described in Algorithm 1. A visualisation of how the estimated *canonical pose* evolves as the volume of the AABB that contains the object decreases is depicted in Figure 5. An advantage of the proposed minimum volume principle is that the recovered *canonical pose* will align one of its coordinate planes with the symmetry plane of the object if it exists.

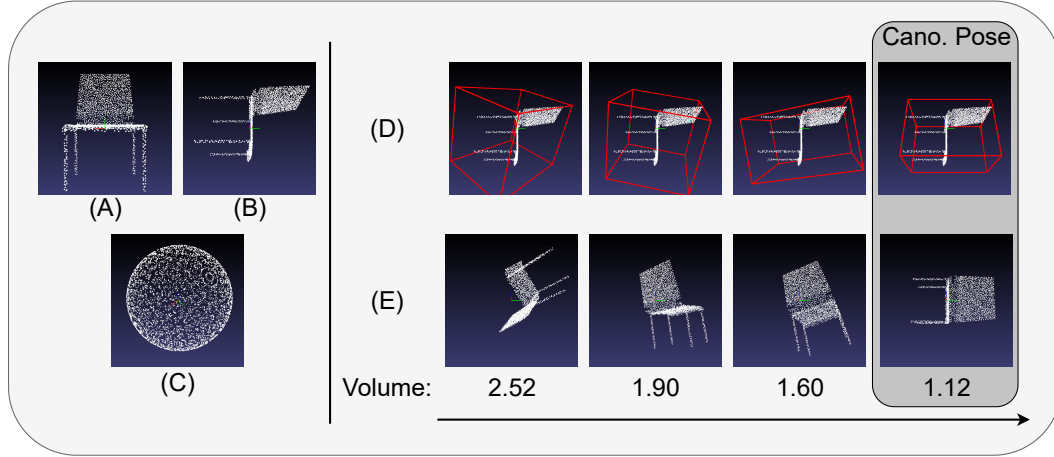


Figure 5: We demonstrate the point cloud of a chair (A) in arbitrary pose (B) and how its *canonical pose* is recovered using the minimum volume principle. The selection matrices \mathbf{R}^s are illustrated in (C) by rotating a point at $[1, 1, 1]$ with all the selection matrices. (D) and (E) depict how the estimated object orientation represented by a bounding box and the object viewed in its *canonical pose* evolve with respect to the volume of the AABB.

Algorithm 1: Minimum Volume Principle

Input: points $\mathbf{P} \in \mathbb{R}^{N \times 3}$ representing the object, and selection rotation matrices $\mathbf{R}^s \in \mathbb{R}^{N_s \times 3 \times 3}$.

Output: translation and rotation parameters $\{\mathbf{T}, \mathbf{R}\}$ that map \mathbf{P} to their canonical coordinates

$\beta \leftarrow 0.01$ ▶ Tolerance hyperparameter
 $\hat{\mathbf{P}} = (\mathbf{R}^s)^{-1} \mathbf{P}$ ▶ Transform points into coordinates with orientations \mathbf{R}^s
 $V = \text{COMPUTE VOLUME}(\hat{\mathbf{P}})$ ▶ Compute volume of AABBs that contain $\hat{\mathbf{P}}$
 $V_{\min} = \min(V)$ ▶ Find smallest volume
 $\hat{\mathbf{R}}^s = \{\mathbf{R}_i^s | V_i \in [V_{\min}, (1 + \beta)V_{\min}]\}$ ▶ Select similar sized AABBs to minimum
 $d_{\text{SO}(3)} = \arccos\left(\frac{\text{tr}(\hat{\mathbf{R}}^s) - 1}{2}\right)$ ▶ Compute geodesic distance to the world frame
 $\mathbf{R} = \hat{\mathbf{R}}_j^s$ with $j = \text{argmin}(d_{\text{SO}(3)})$ ▶ Find AABB closest to the world frame
 $\mathbf{T} = \frac{1}{N} \sum_{i \in \{1, \dots, N\}} \mathbf{p}_i$ with $\mathbf{p}_i \in \mathbf{P}$ ▶ Compute centre of mass for points

6.2 Training and Implementation Details

Training takes about 35 hours for the YCB video dataset and 20 hours for the YCB static dataset on a single NVIDIA Titan RTX GPU. The video model and the static model are trained for 100k and 100.5k iterations, each with a batch size of 2 and 8, respectively, selected according to the available GPU memory. The IC-SBP ablation has a batch size of 8 for the video experiments as it's a static image-based approach. For ObSuRF, we train for 90k and 100.5k with a batch size of 32 for the video and static image data. Video length is 5 frames randomly cropped from the full video for training and we use the full video length (typically 15 frames or longer) for testing. The model is thus able to process videos that are much longer than the videos seen during training. The YCB video dataset

has 4000 videos for training and 500 videos for testing. The YCB static dataset has 12000 scenes for training and 1500 scenes for testing. We summarise all the hyper-parameters in Table 2. In the ablation study we use slot attention with a background slot as introduced in Yu et al. [12]. For video data, slots from the last time step are used to initialise slot attention at the current time step. For both datasets, OBPOSE estimates the canonical poses with all points below the ground surface being neglected, as we find that NeRF can mistakenly predict the occupancy of the points below the ground surface whose x-y coordinates are within the object’s convex hull. This (erroneous) generalisation follows from the fact that this part of the scene receives no training signal, due to the ray marching used in NeRFs.

6.3 Network Structures

The KPConv encoder backbone consists of an input block and three consecutive encoding blocks with radiuses of [0.025, 0.05, 0.1, 0.2] meters for the KPConv layers. Each block has three sub-blocks which each has a structure of *Conv1d-Group norm*[54]-*ReLU-KPConv-Conv1d-Group norm-ReLU* with a skip connection being built between the output of the first ReLU layer and the output. The skip connection takes the output of the ReLU and feeds it into a Conv1d layer followed by a Group norm. The input block consists of an input layer of *KPConv-Group norm-ReLU* and a single sub-block as described above. For the input block and all the sub-blocks, the number of channels are [16, 16, 32, 32, 32, 64, 64, 64, 64, 64, 64, 64] respectively and the strides are [8, 1, 4, 1, 1, 4, 1, 1, 4, 1, 1]. The KPConv-aggregate layer has a channel number of 64 and a radius of 1 meter. Two trilinear interpolation layers are used to up-sample the embedding and predict embedding of 64 channels and 32 channels respectively. A *Conv1d-Group norm-ReLU* encoding is used in both the input and the skip connection between the input and the output of the interpolation layer. A final output layer of structure *Conv1d-Group norm-LeakyReLU(0.1)-Conv1d* is appended to the output embedding with channel numbers of 32 and 16 for the two Conv1d layers. The *where* encoder and the *what* encoder share the same structure of the backbone encoder and have channel numbers of [16, 16, 32, 32, 32, 64, 64, 64, 64, 64, 64] and strides of [1, 1, 4, 1, 1, 4, 1, 1, 4, 1, 1]. A final output layer of structure *Linear-Group norm-LeakyReLU(0.1)-Linear* is used to predict the final embedding. Both linear layers have 64 output channels. The RNNs used to parameterise the posterior and the prior distribution of the *where* and the *what* latent embedding has a dimension of 32 for the hidden state followed by an MLP of size [32, 32, 64] with the output 64 channels being further divided into the mean and the standard deviation of the Gaussian. The \mathbf{z}^{where} is decoded into the $\Delta\mathbf{T}$ using an MLP of sizes [32, 256, 3]. We use the default NeRF decoder open-sourced by Niemeyer and Geiger [28].

Table 2: Hyperparameters of OBPOSE.

Parameter	Description	Value
σ_{std}	Standard deviation of colour dist.	0.1
σ_{max}	Maximum density	10
s	Bounding box size	0.4
N_{thresh}	Number of points to use the pose of last time step	10
T_{max}	Maximally allowed $\Delta\mathbf{T}$	0.1
\mathbf{S}	Number of sparse voxels along each dimension	24
δ	Noise added to depths $d_{surface}$	0.01
β	tolerance factor to select minimum volume bounding box	0.01
K	Number of slots for IC-SBP	4
d_z	Dimensionality of both \mathbf{z}^{where} and \mathbf{z}^{what}	32

6.4 Segmentation Results on YCB Static

We illustrate additional segmentation results on YCB static dataset in fig. 6.

6.5 Limitations and Potential Societal Impact

The present work advances the state-of-the-art in unsupervised 3D-scene segmentation and interpretation. While OBPOSE is important for advancing research, its impact outside of the machine learning community is low as current methods can not yet deal effectively with real images. This highlights the current limitations of the proposed model. In the future, we will investigate how to build a model

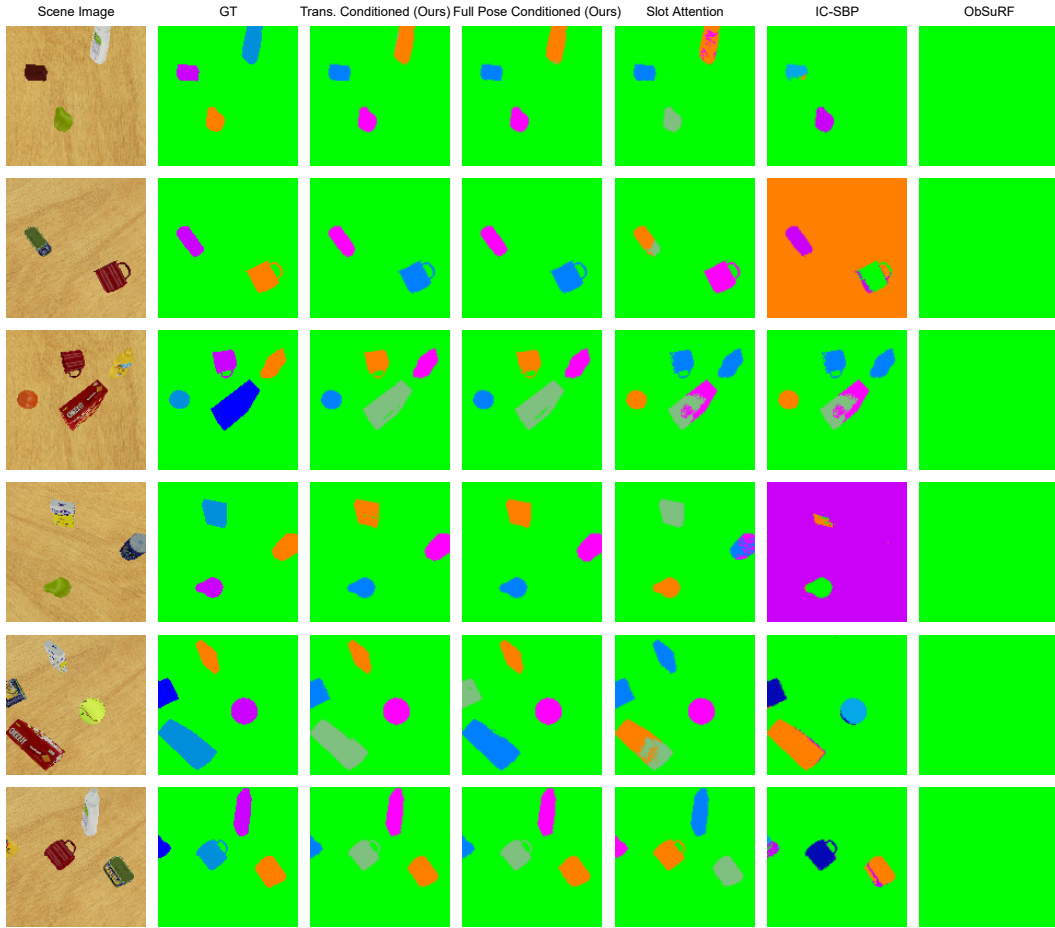


Figure 6: Qualitative results on YCB static dataset.

that can explain complex real-world observations including e.g. shadows. OBPOSE will then be ready for real-world robotics applications as a vision backbone.